



Importance of rigidity of ice-binding protein (*Ff*IBP) for hyperthermal hysteresis activity and microbial survival

Jisub Hwang^{a,b,1}, Bomi Kim^{a,b,1}, Min Ju Lee^a, Eun Jae Kim^c, Sung Mi Cho^c, Sung Gu Lee^{a,b}, Se Jong Han^{b,c}, Kitae Kim^{a,b,*}, Jun Hyuck Lee^{a,b,*}, Hackwon Do^{a,b,*}

^a Research Unit of Cryogenic Novel Material, Korea Polar Research Institute, Incheon 21990, Republic of Korea

^b Department of Polar Sciences, University of Science and Technology, Incheon 21990, Republic of Korea

^c Division of Life Sciences, Korea Polar Research Institute, Incheon 21990, Republic of Korea

ARTICLE INFO

Keywords:

Polar microorganisms
Ice binding proteins
Cold adaptation

ABSTRACT

Ice-binding proteins (IBPs) are well-characterized proteins responsible for the cold-adaptation mechanisms. Despite extensive structural and biological investigation of IBPs and antifreeze proteins, only a few studies have considered the relationship between protein stabilization and thermal hysteresis (TH) activity as well as the implication of hyperactivity. Here, we investigated the important role of the head capping region in stabilization and the hyper-TH activity of *Ff*IBP using molecular dynamics simulation. Data comparison revealed that residues on the ice-binding site of the hyperactive *Ff*IBP are immobilized, which could be correlated with TH activity. Further comparison analysis indicated the disulfide bond in the head region is mainly involved in protein stabilization and is crucial for hyper-TH activity. This finding could also be generalized to known hyperactive IBPs. Furthermore, in mimicking the physiological conditions, bacteria with membrane-anchored *Ff*IBP formed brine pockets in a TH activity-dependent manner. Cells with a higher number of TH-active IBPs showed an increased number of brine pockets, which may be beneficial for short- and long-term survival in cold environments by reducing the salt concentration. The newly identified conditions for hyper-TH activity and their implications on bacterial survival provide insights into novel mechanistic aspects of cold adaptation in polar microorganisms.

1. Introduction

Ice grows from ice crystal seeds and expands its size as temperature drops. The ice size can be increased even under diminutive temperature fluctuations—known as ice recrystallization [1,2]. Ice formation and growth in the inner and outer layers of cells cause physical damage as well as osmotic shock to organisms in sub-zero environments [3–5]. Therefore, organisms from the polar region produce ice-binding proteins (IBPs) or antifreeze proteins (AFPs) to protect themselves from freeze-induced damage as cold adaptation and/or avoidance mechanisms² [6].

Unlike general enzymes, IBPs have unique properties, i.e., binding to

ice, and this interaction results in the inhibition of ice growth at low temperatures by covering the potential binding sites for water molecules on the crystal surface [7]. The magnitude of the interaction strength can primarily be evaluated using the thermal hysteresis (TH) activity and an ice recrystallization inhibition assay [8]. The TH activity is represented by a numerical value defining the gap between the freezing and melting points. Based on TH activity, IBPs can be divided into two groups: moderately active or hyperactive IBPs. Moderately active IBPs have been found in fish and plants with TH activity of ~0.5 °C at the maximum protein concentrations measured, whereas the hyperactive proteins from bacteria and insects show activity up to 5 °C at the

Abbreviations: AFP, antifreeze protein; ESID, electronically switchable illumination and detection; FITC, fluorescein isothiocyanate; IBP, ice-binding protein; IBS, ice-binding site; LB, Luria-Bertani; MD, molecular dynamics; PBS, phosphate-buffered saline; QLL, quasi-liquid layer; RMSD, root mean square deviation; RMSF, residual root mean square fluctuation; SD, steepest descent; TH, thermal hysteresis.

* Corresponding authors at: Research Unit of Cryogenic Novel Material, Korea Polar Research Institute, Incheon 21990, Republic of Korea.

E-mail addresses: ktkim@kopri.re.kr (K. Kim), junhyucklee@kopri.re.kr (J.H. Lee), hackwondo@kopri.re.kr (H. Do).

¹ These authors contributed equally to this work.

² Although the term AFPs is more specific to proteins that have thermal hysteresis (TH) activity and/or ice recrystallization inhibition (IRI) activity [34,48], the term IBPs covers a wider concept, representing the function of the proteins and encompass the previously identified IBPs and AFPs. Thus, the term IBPs is used in this paper to explain proteins with ice growth inhibition activity, except for proper nouns [1].

<https://doi.org/10.1016/j.ijbiomac.2022.02.032>

Received 24 November 2021; Received in revised form 5 February 2022; Accepted 7 February 2022

Available online 9 February 2022

0141-8130/© 2022 Published by Elsevier B.V.

maximum concentration [9–13]. Two factors are common for hyperactive proteins: a common motif at the ice-binding site (IBS) and a wide range of IBSeS [14]. For example, the hyperactive *TmAFP* from *Tenebrio molitor* and *sbwAFP* from the spruce budworm (*Choristoneura occidentalis*) contain regular Thr-X-Thr motifs at the IBS, whereas *MpAFP* from *Marinomonas primoryensis* contains the Thr-X-Asn motif [9,15,16]. These regularly spaced residues can be assembled with an ice lattice, probably via the ordered hydration layer of water molecules. In addition, these hyperactive IBPs are formed by the association of parallel β -strands in a helical pattern. This parallel β -sheet is beneficial for hyperactive IBPs to interact with an extended ice surface. Furthermore, truncated *CfAFP* (from *C. fumiferana*) showed reduced TH activity, whereas long wild-type *CfAFP* had a higher activity, indicating that the area of IBP interacting with ice is vital for hyper-TH activity [14].

The binding mechanism between IBPs and ice has been established using multiple methods [17], and the dominant theory states that IBPs interact with ice via water-mediated interactions involved in hydrogen bonding and hydrophobic effects coordinating water molecules at the IBS. In other words, residues on the IBP surface play a role in arranging the water molecules, which mimics the arrangement of water molecules on ice [18–20]. Thus, well-arranged and rigid residues at IBSeS complementary to ice water would be important to increase the ice-binding strength of IBPs, as shown in the hyperactive IBPs. However, although intensive biochemical and structural investigations of IBPs have been conducted for decades, information regarding the correlation between the structural stability and TH activity as well as the implication of hyperactive IBPs for microbial survival in cold environments is limited.

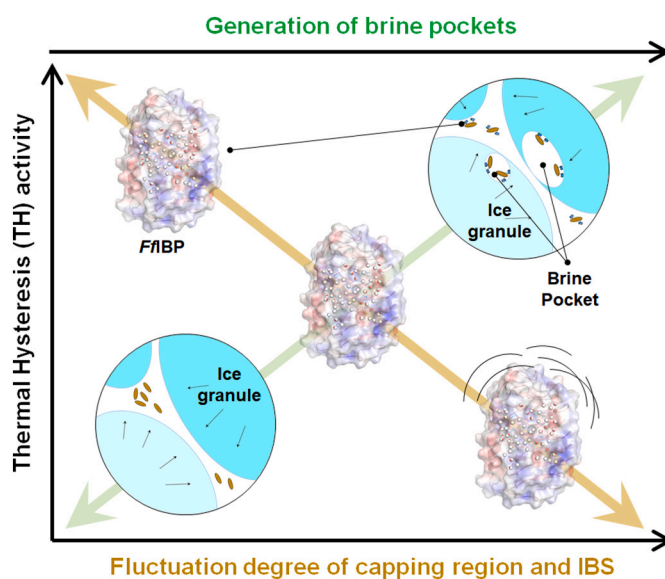
Previously, our lab investigated two IBPs, *FfIBP* from the Antarctic bacterium *Flavobacterium frigidis* PS1 and *LeIBP* from the Arctic yeast *Glaciozyma* sp. [10,21–23]. Although the two IBPs share a highly sequential and tertiary structure similarity, the TH activity of *FfIBP* was 10 times higher than that of *LeIBP*. The residue composition (e.g., T-A (G)-X-T/N motif at the IBS) and broader surface area at the IBS were thought to be important factors for the hyperactivity of *FfIBP* [10]. However, although the chimeric protein *mFfIBP*, whose capping head region with *LeIBP* is swapped, has highly identical residues at the IBS similar to *FfIBP*, it showed only moderate TH activity and lower stability than *FfIBP*. Based on this observation, we hypothesized that the capping head region is important for TH activity by stabilizing the overall structure.

Herein, we report that the capping head region of β -helical IBPs is involved in protein stabilization that can be correlated to the hyper TH activity. Hyperactive IBPs have either *FfIBP*-like capping head region or disulfide bond in the ice interacting strands for protein stabilization. Importantly, we show that polar microorganisms utilize the hyperactive and membrane-anchored IBPs that promote the formation of brine pockets to reduce the salt concentration in the sub-zero environments (Scheme 1).

2. Results and discussion

2.1. Capping head region-dependent TH activity

Although the ice crystal plane where *FfIBP* can bind has not been identified experimentally, the docking experiment and the dendritic pattern perpendicular to the c-axis at the freezing point clearly indicate that *FfIBP* binds to the basal plane [10,21]. To facilitate the interaction between *FfIBP* and ice, *FfIBP* comprises T-X-A-T(N) motifs at the IBS; these motifs are flat with parallel β -strands [21]. In particular, the residues forming the motifs T79-X-A-T82 on β 2, T263-X-A-T266 on β 17, and T245-X-A-T248 on β 15 (X: Val or Ile) matched the regularly spaced water molecules on the basal plane of ice crystals (Fig. 1A) [21]. This positional combination of motifs was also found in the hyperactive IBPs for favorable contact with either the hydration water or water from ice and is thought to be an important factor for hyper-TH activity [11,14,24].



Scheme 1. Schematic illustration of the negative correlation between fluctuation and TH activity of *FfIBP* and mechanistic insights into cold adaptation for hyperactive *FfIBP* anchored on microorganism membrane. *FfIBP* is shown in surface presentation, and the ordered hydration water layer around the IBS is shown with spheres (white for hydrogen and red for oxygen). Brine pocket formation (large white ovals) caused by *FfIBPs* attached to the microorganism (small brown ovals) is shown in a circle. (For interpretation of the references to color in this figure legend, the reader is referred to the web version of this article.)

Previously, we generated chimeric protein (*mFfIBP*), whose sequence was a combination of capping region (a.a. 62–109) from *LeIBP* and body region (a.a. 2–61 and 110–255) from *FfIBP*, and determined the crystal structure at 2 Å resolution (PDB code: 4NU3) [21]. The structural comparison of *FfIBP* with *mFfIBP* showed that the *mFfIBP* body region (61–92 and 130–276) was similar to *FfIBP* with a root-mean-square deviation (RMSD) of 0.30 Å for C α and near identical for residues of β 2, β 15, and β 17 at the IBS (Fig. 1C and S1 Fig. and S2 Fig.). The only difference between *FfIBP* and *mFfIBP* is the capping head region. Although the IBSeS of both proteins are similar, their activity is different. The TH activity of *FfIBP* is close to 2.5 °C at 50 μ M concentration [10]. In contrast, the TH activity of *mFfIBP* was three times less than that of *FfIBP*, indicating that the composition of the residues at the IBS was not a sufficient criterion for hyperactivity, and some other factor (s) from the capping head region may be influencing TH activity. The capping head region-dependent TH activity was consistent with the single mutation C107S in the capping head region. Breaking the disulfide bond by mutation resulted in decreased activity, indicating that rigidity in the capping region may be an essential factor in maintaining the hyperactivity of *FfIBP* (Fig. 1D and S3 Fig.).

2.2. Residual fluctuation at IBS caused by capping head region

As observed in the hyperactive IBPs, regularly spaced motifs seem critical for hyperactivity [25]. Water molecules on the basal plane of ice, where the hyperactive IBPs mainly interact, were spaced 4.5 Å vertically and 10.5 Å horizontally. At the IBS of *FfIBP*, the distance between T79 and T245 and between T82 and N248 was 9.7 Å and 8.9 Å (C β), respectively, and the distances between T79 and T82 and between T245 and N248 were close to 10 Å (C β) for both, which stereo-specifically matches the basal plane of the ice (S4 Fig.) [21]. In addition, the electrostatic potential was analyzed using the Adaptive Poisson-Boltzmann Solver to understand the ice-binding mechanism of *FfIBP* [26]. The analysis revealed that the IBS of *FfIBP* consists of mainly non-polar residues, whereas the negatively charged residues from the motifs are

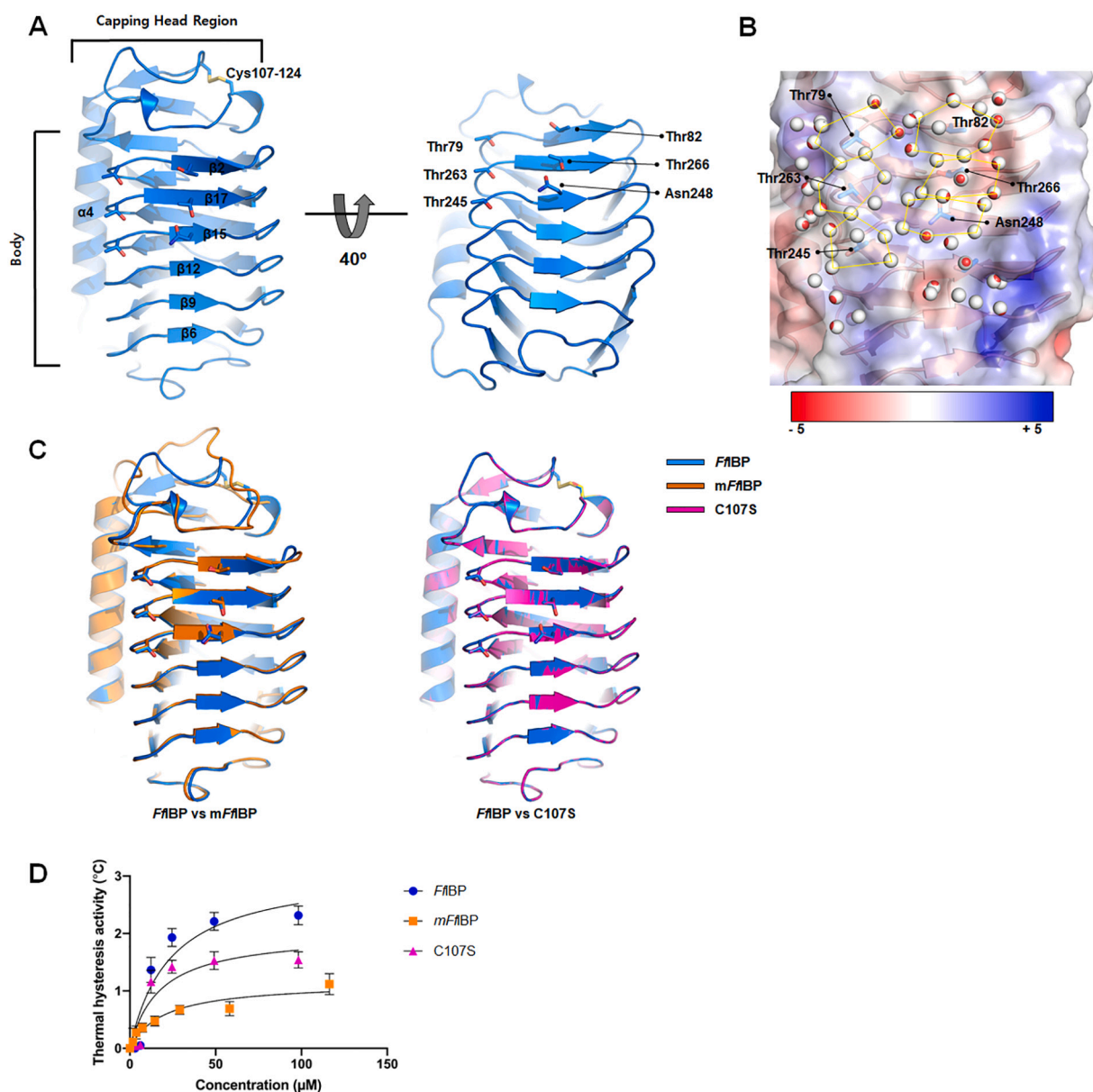


Fig. 1. Structure and activity comparison of *FfIBP* with derivatives. (A) Cartoon view of *FfIBP* with forward-facing IBS. Ice-binding motifs on $\beta 2$, $\beta 17$, and $\beta 15$ are represented with sticks with CPK coloring. (B) Structure superposition of *FfIBP* with *mFfIBP* and C107S. (C) TH activity of *FfIBP*, *mFfIBP*, and C107S at different concentrations.

locally distributed (Fig. 1B). This hydrophobic surface with spaced hydroxyl groups from the motifs is considered an important feature of IBS for stabilizing the hydration water layer ordering, which is associated with its ice-binding function. Consistent with this observation, careful investigation regarding the hydration water layer on IBS found the hexagonally latticed water molecules around the residues from the motifs after solvation and energy minimization during simulation [27]. The reduced activity of *mFfIBP* or C107S is probably due to the disturbance of these hydration water molecules on the IBS, which stems from the capping head region of *FfIBP*. Based on this idea, we hypothesized that the immobility of *FfIBP* is important for interaction with solid ice. To test this hypothesis, we performed molecular dynamic (MD) simulations using *FfIBP*, C107S, and *mFfIBP* structures.

First, the RMSD and residual root-mean-square fluctuation (RMSF) were calculated for each system to measure the spatial fluctuation of residues at the IBS from the MD simulation at 300 K. The mean RMSD of *FfIBP* during simulation was below 0.9 Å with a low standard deviation (0.108 Å), whereas the RMSD of *mFfIBP* and C107S was close to or

higher than 1 Å as 1.23 Å and 1.18 Å, respectively. In contrast to *FfIBP*, the RMSD of *mFfIBP* and C107S continued to increase over time, indicating higher fluctuations in residue positions around the starting points (Fig. 2A). Furthermore, the RMSD difference was caused by residual movement in the capping head region of the IBPs in both cases.

A comparison of *FfIBP* with *mFfIBP* indicated that the a.a. 70–80 region of *mFfIBP* was more mobile, as indicated by the high value of fluctuation in the simulation data (Fig. 2B). Superimposition of the frames extracted from *mFfIBP* simulation every 10 ns exhibited notable flexibility at the small turn region (70-PAAAY-75). This alanine-rich region was barely connected via hydrophobic interaction between Ala73 and Tyr104 in the crystal structure. The simulation result indicated that the interaction between the two residues is disrupted, and the PAAAY region could be freely flipped out toward the IBS. This would generate steric hindrance which may interfere with the IBS's access to the ice, resulting in the loss of TH activity (Fig. 3B). Notably, the capping head region fluctuation was also observed in the C107S system. The distance of alpha-carbons between C107 and C124 of *FfIBP* is close to

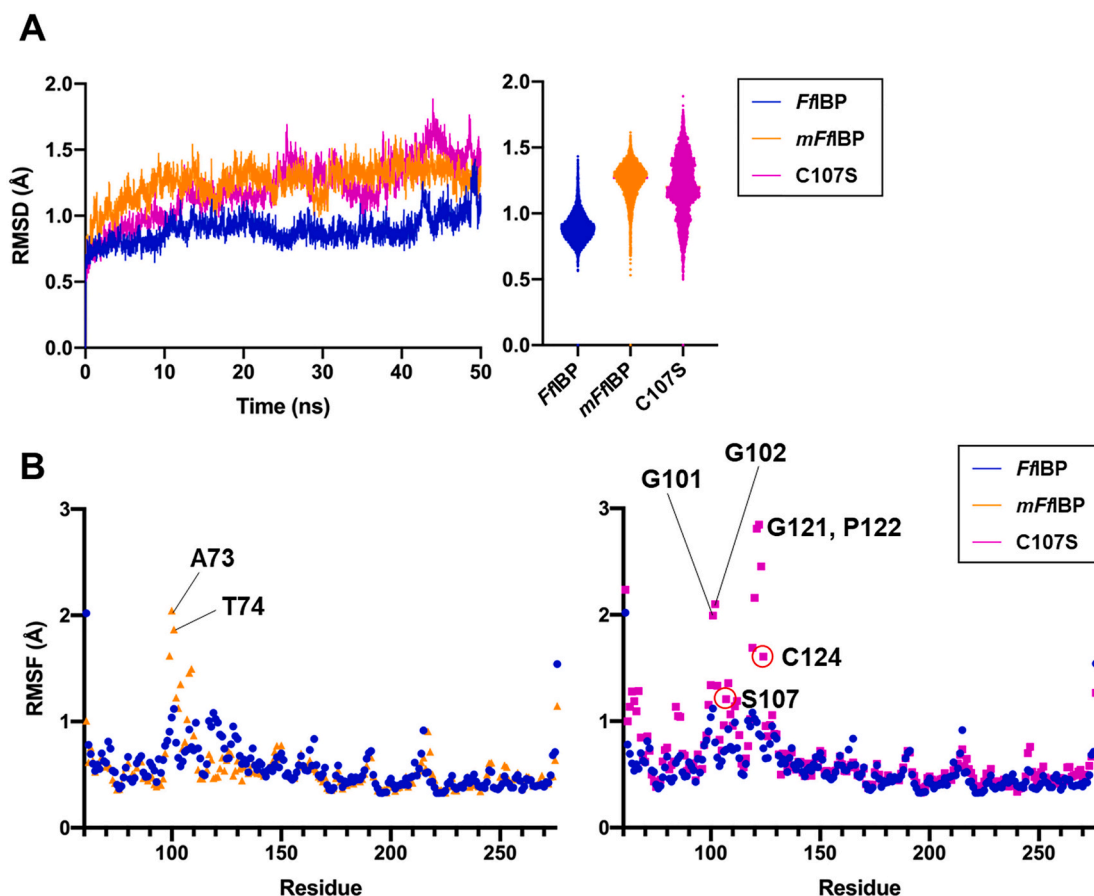


Fig. 2. MD simulation and residual fluctuation. (A) Backbone RMSDs ($C\alpha$) of *FfIBP* (blue), *mFfIBP* (orange), and C107S (magenta). (B) Backbone RMSF ($C\alpha$) of each residue as a function of the atom location along with the proteins. (For interpretation of the references to color in this figure legend, the reader is referred to the web version of this article.)

3.7 Å, which does not change during simulation. However, breaking the disulfide bond by mutation (C107S) resulted in a great increment in the distance from 3.7 Å to 8.3 Å (at 50 ns) between Ca of two cysteines and displacements of Cys124. This fluctuation at the unstructured loop influenced the movement in the 98-ITGAA-102 region that corresponds to the PAAAY region of *mFfIBP*. Together, the switching of the capping head region or breaking the disulfide bond (C107–C124) resulted in an increased fluctuation of the entire capping region of IBP, specifically the small turn region facing the IBS (Fig. 3C).

Next, we investigated how the movement of the capping head region reflects at the IBS. The investigation of the residual movement in the IBS implied that a mutation in the capping head region distorts the position of residues. The distance of the grid-like position of the hydroxyl residues was measured from the simulation data. The average distance between T79 and T245 of *FfIBP* was 10.36 Å during the entire simulation, which is almost identical to the vertical distance of water molecules on ice. However, the *mFfIBP* and C107S showed increased distance, with mean distances of 11.25 Å and 11.20 Å, respectively (Fig. 4A and S3 Table). It is also worth noting that the distance between T79 and T82 of *FfIBP* was steady with a low standard deviation during the simulation, whereas that of *mFfIBP* and C107S increased with time, indicating the increased movement of residues (Fig. 4A). However, the distances that involved N248 (i.e., T82–N248 and T245–N248 for *FfIBP* and C107S; T55–N228 and T225–N228 for *mFfIBP*) were similar to those of *FfIBP*. Therefore, T79 was the most affected residue from the capping head region fluctuation with a tendency to move toward the capping head region (Fig. 4A).

As the arrangement of the hydration water molecules in regular intervals is essential and is thought to play an important role in facilitating

IBP binding, we analyzed the side-chain dihedral angle distributions of motifs interacting with the hydration water. The dihedral angles (χ_1) of T79 (T52 of *mFfIBP*), T82 (T55 of *mFfIBP*), T245 (T225 of *mFfIBP*), and N248 (N228 of *mFfIBP*) were measured and compared [28]. The dihedral angle distributions showed that the side chain of T79 of *FfIBP* is steady, as indicated by a major peak at 60° with a low deviation, whereas the T52 of *mFfIBP* and T79 of C107S changed the dihedral angles with a high deviation. In a comparison of T82s, although *FfIBP* and *mFfIBP* exhibited similar distribution angles at 180° as major peaks, a minor peak could also be seen at 60° for *mFfIBP* (T55). Moreover, unlike *FfIBP* and *mFfIBP*, the T82 of C107 showed dominant rotamers at different angles. These distribution differences were also seen in T245 and T248. In case of T245, the preferred orientation of *FfIBP* was 60°, whereas the *mFfIBP* and C107S changed the orientation approximately to 160° and 180°, respectively. Moreover, major peaks for N248 distribution had not changed among IBPs, but the minor peaks for *mFfIBP* and C107S were increased at 180° (Fig. 4B). The distance between two residues and the rotamer distribution analysis indicate that the fluctuation of the capping head region alters the movement of residue as well as the side-chain conformation that are essential for the arrangement of hydration water molecules on IBS. Together, these results indicate that the capping head region with the disulfide bond of *FfIBP* influences the immobilization of the residues at the IBS.

2.3. Morphology of ice crystals in the presence of IBPs

The ice morphology and growth rate were checked at a freezing point during the TH activity measurement. *FfIBP* effectively and consistently inhibited ice growth until the ice burst rapidly. Dendritic burst

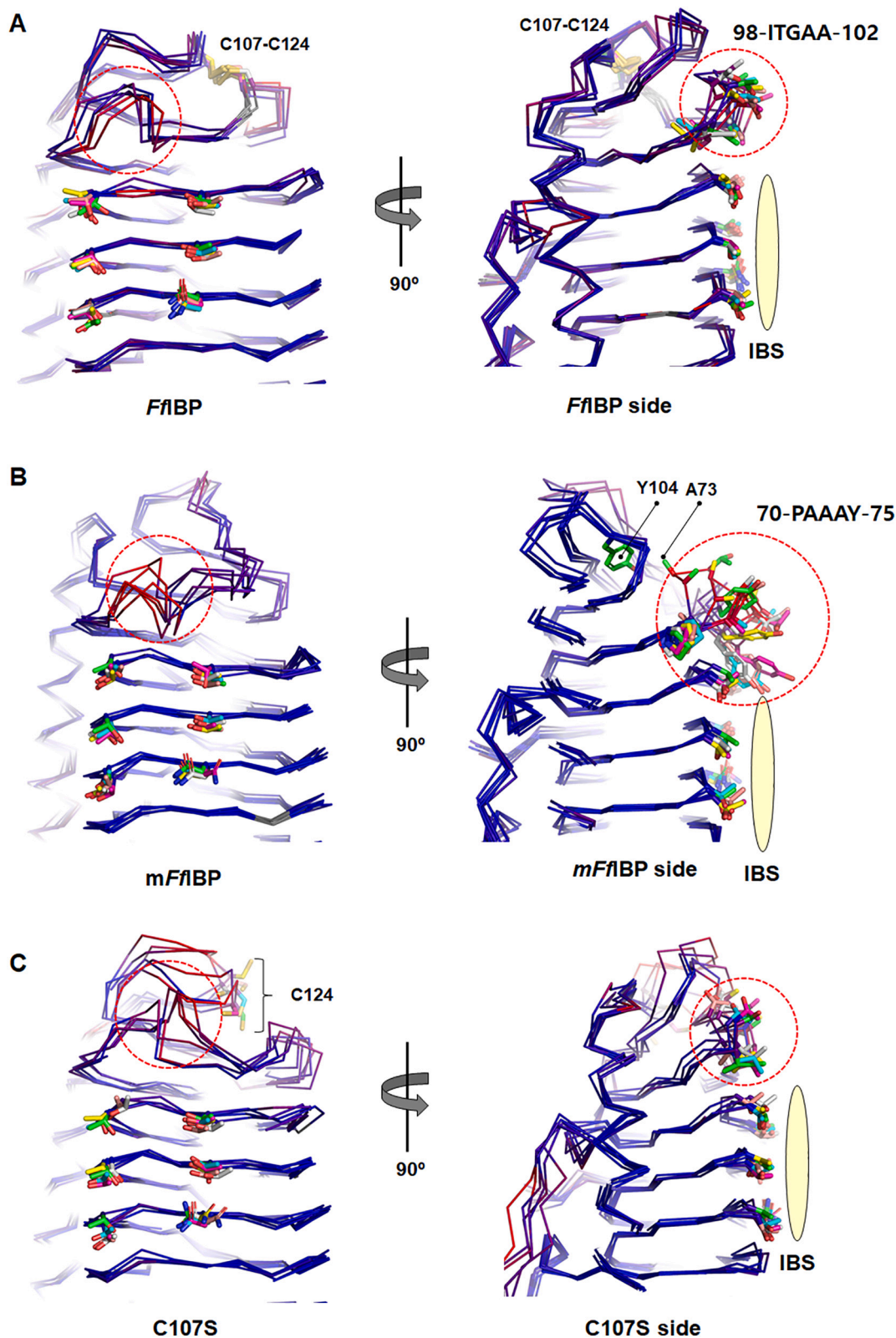


Fig. 3. Superposition of the initial structure and frames extracted from *FfIBP* (A), *mFfIBP* (B), and *C107S* (C) simulation system. The initial structure was used as a target, and every 10 ns frame was aligned as mobile. Each mobile/target atom-pair was colored by distance. Dark blue indicates good alignment, while red means higher deviations. The motifs on IBS and the capping head region residues of 98-ITGAA-102 of *FfIBP* and C107 and 70-PAAAY-75 of *mFfIBP* are represented by sticks with different color codes. The IBS is shown with a light yellow oval. (For interpretation of the references to color in this figure legend, the reader is referred to the web version of this article.)

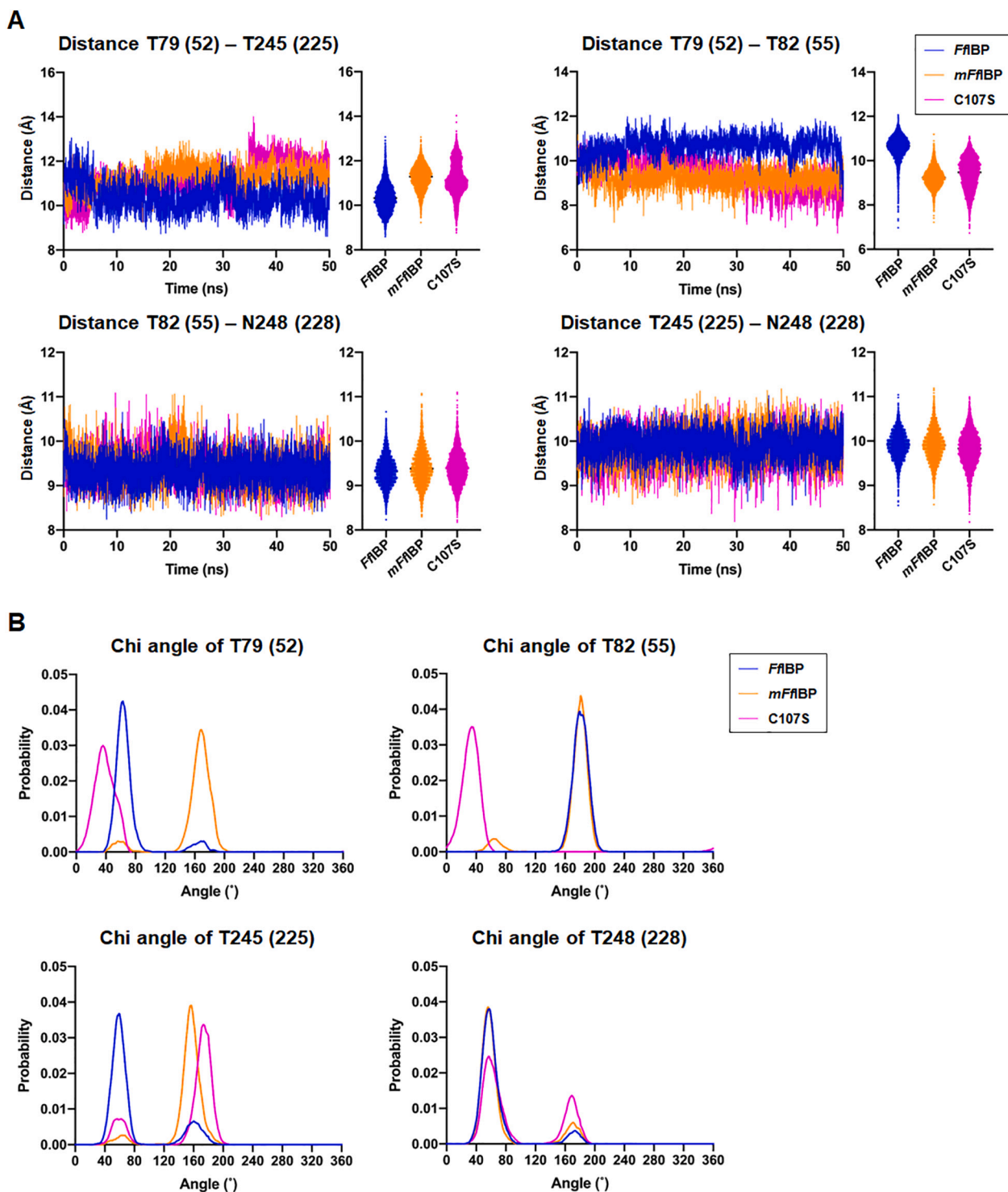


Fig. 4. Capping head region-dependent movement during MD simulations. (A) Distance ($C\beta$) of two residues at IBS and magnitude of fluctuation for WT (blue), *mFfIBP* (orange), and C107S (magenta) during MD simulations. Distances between the residues (T79–T245), (T79–T82), (T82–N248), and (T245–N248) for *FfIBP* and C107S and (T52–T225), (T52–T55), (T55–N228), and (T225–N228) for *mFfIBP* were measured during the simulation. The mean distances and distribution of each combination of residues are shown on the right panel with the same color code. The distances were calculated from the trajectory files taken every 10 ps from MD simulation. (B) Side-chain dihedral angle distribution (χ_1) of T79, T82, T245, and N248 of *FfIBP* and C107S, and T52, T55, T225, and N228 of *mFfIBP*. Dihedral angle of N-Ca-C α -CG2 for Thr and N-Ca-C α -CG for Asn were measured, and the probability was displayed as a function of angle. Corresponding residues in *mFfIBP* were shown in brackets. (For interpretation of the references to color in this figure legend, the reader is referred to the web version of this article.)

formation is a typical phenomenon of hyperactive IBPs because they mainly bind to the basal plane such that the ice grows along the A-axis [29–33]. However, *mFfIBP* and C107S failed to inhibit the ice growth, even at higher concentrations (Fig. 5). This observation provides

convincing insights regarding the low TH activity of *mFfIBP* and C107S. Other differences in the presence of *mFfIBP* and C107S were ice morphologies. Ice forms truncated bipyramidal structures in the presence of *mFfIBP*, whereas ice with C107S shows hexagrams. The hexagram

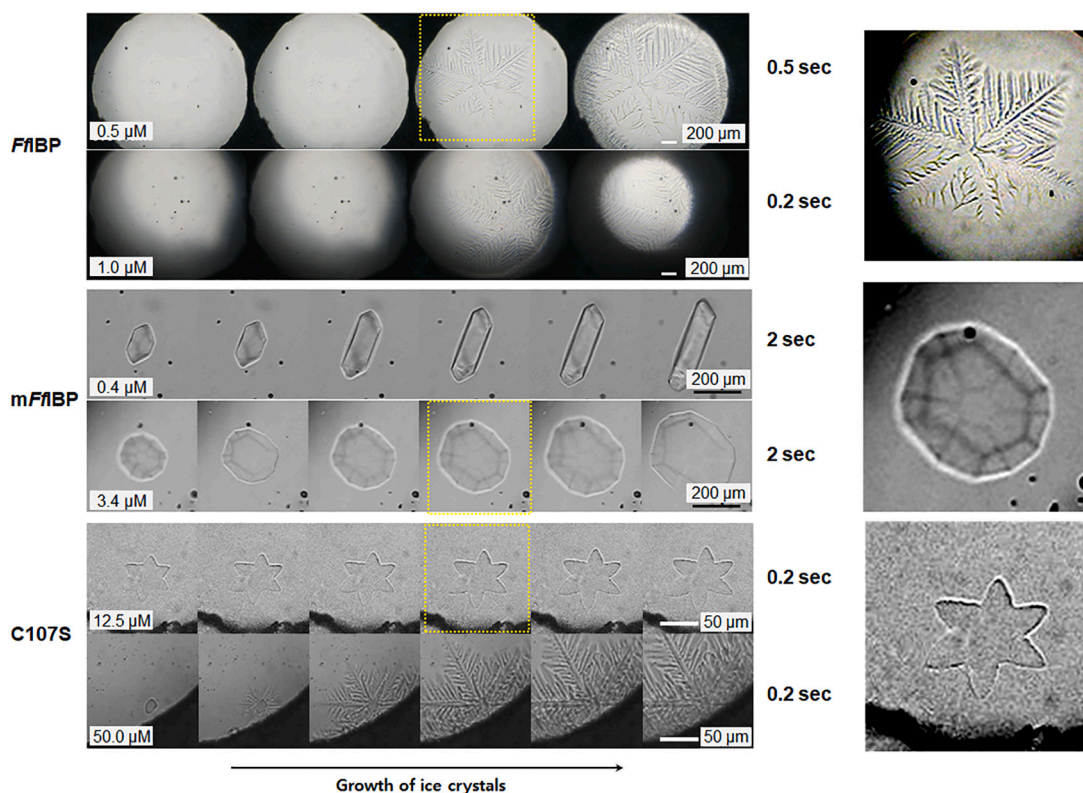


Fig. 5. Ice morphology at different concentrations at the freezing points of *FfIBP*, *mFfIBP*, and *C107S*. *FfIBP* effectively and consistently inhibited the growth of ice until the ice burst, whereas *mFfIBP* failed even at higher concentrations. The pictures were taken during the TH measurement. The time interval is indicated on the right side of the pictures. Photographs were taken using a Canon Power Shot 620. (Right panel) Magnified view of each ice crystal from yellow square. The scale bars represent 200 μm , 200 μm , and 50 μm for *FfIBP*, *mFfIBP*, and *C107S*, respectively. (For interpretation of the references to color in this figure legend, the reader is referred to the web version of this article.)

formation changed at a higher concentration of *C107S*, similar to the ice morphology in the presence of *FfIBP*. The residue composition on IBS of *mFfIBP* and *C107S* were well fitted to the corresponding residues on IBS of *FfIBP*. However, the increase in residue mobility might have disrupted or weakened the bonding between the protein and ice, resulting in

differences in the ice growth rate and morphology of *FfIBP*, *mFfIBP*, and *C107S* (Fig. 5).

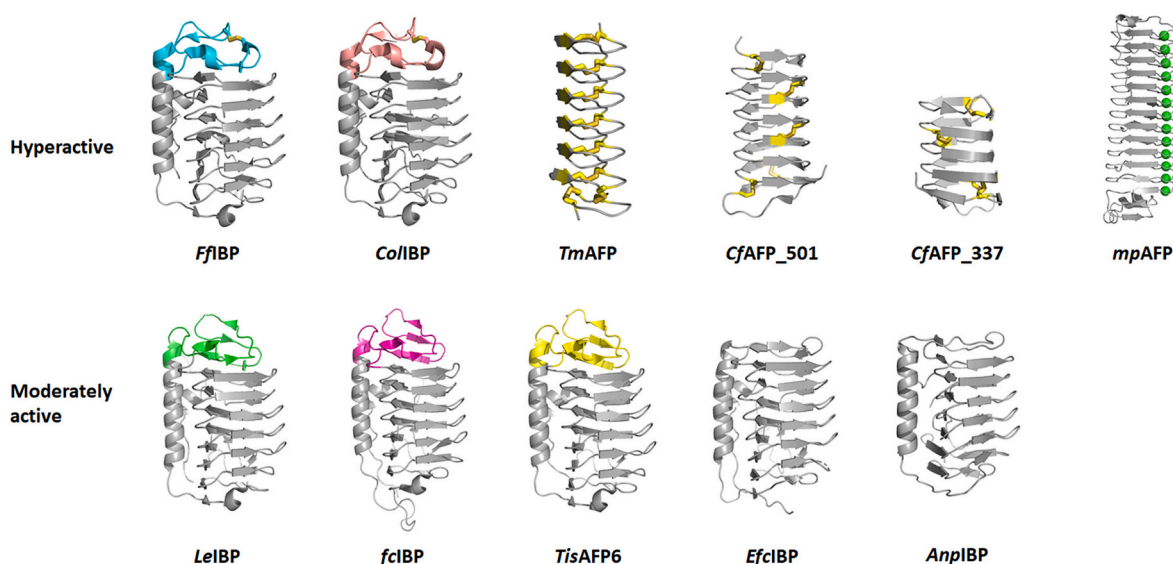


Fig. 6. Representations of the overall structure of hyperactive and moderately active IBPs. The disulfide bond(s) on the capping head region or in the intermolecular β -strands of the hyperactive IBPs are represented with bold yellow sticks. The moderately active IBPs either have a *LeiBP*-like capping head region or no capping head region. The capping head regions of IBPs are highlighted with different color codes. The green spheres on the structure of *MpAFP* represent calcium ions. (For interpretation of the references to color in this figure legend, the reader is referred to the web version of this article.)

2.4. Common characteristics of hyperactive IBPs or AFPs

To generalize our findings, we analyzed the structural characteristics of the IBPs. Although the IBPs share the same function of adsorption to ice, their structures are diverse [34]. Among them, a particular IBP family with the DUF3494 domain has been consistently found in polar microorganisms. The members of this DUF3494 IBP family include *FfIBP* (PDB:4NU2), *LeIBP* (PDB:3UYV), *CoIAFP* (PDB:3WPY), *TisAFP6* (PDB:3VN3), *EfcIBP* (PDB:6EIO), *CfAFP-501* (PDB:1M8M), *CfAFP-337* (PDB:1LOS), *SfIBP_1* (PDB:6BG8), and *AnpIBP* (PDB:7BWX) [31]. The structural analysis of the IBPs indicated that the DUF3494 IBP family can be divided into two subgroups based on the folding of the capping head region and the presence of disulfide bonds (which always resulted in hyperactive IBPs, except for *TisAFP8*) [19,31]. For example, the hyperactive *CoIAFP* from *Colwellia* sp. SLW05 has similar folding in the capping head region to *FfIBP* with disulfide bonds, whereas other DUF3494 IBPs showing moderate TH activity do not have a disulfide bond or capping head region (e.g., *EfcIBP* and *AnpIBP*) [33,35] (Fig. 6). Notably, *SfIBP_1* with distinctly different folding in the capping head region from the two subgroups has TH activity between moderate and hyperactivity, indicating that the folding of the capping head region is

probably a distinguishable factor for TH activity [31].

Furthermore, in this study, although the hyperactive IBPs do not belong to the DUF3494 IBP family, they have intramolecular disulfide bonds in the intervals of the β -strands at the IBSEs. The disulfide bond among the strands stabilizes the overall structure and helps maintain the rigidity of regularly spaced residues. Therefore, these hyperactive IBPs probably evolved by integrating the disulfide bonds to stabilize the structure, resulting in hyperactivity. In contrast, the hyperactive *MpAFP*, which does not have a disulfide bond, instead has calcium ions between β -strands for the regular interval of residues. This contradicts the importance of rigid and regularly spaced residues for hyperactivity (Fig. 6) [15].

The data presented herein indicate that the stability of regularly spaced residues at the IBS stemming from the capping head region is an essential factor for the hyperactivity of *FfIBP*, which had been less focused for TH activity, whereas the composition of hydrophilic residues and shape of the IBS have received attention. Furthermore, generalizing our findings to the DUF3494 IBP family and β -helical hyperactive IBPs suggests that either the capping head region or integrated disulfide bond (s) of IBPs seems to be an important factor for hyper-TH activity.

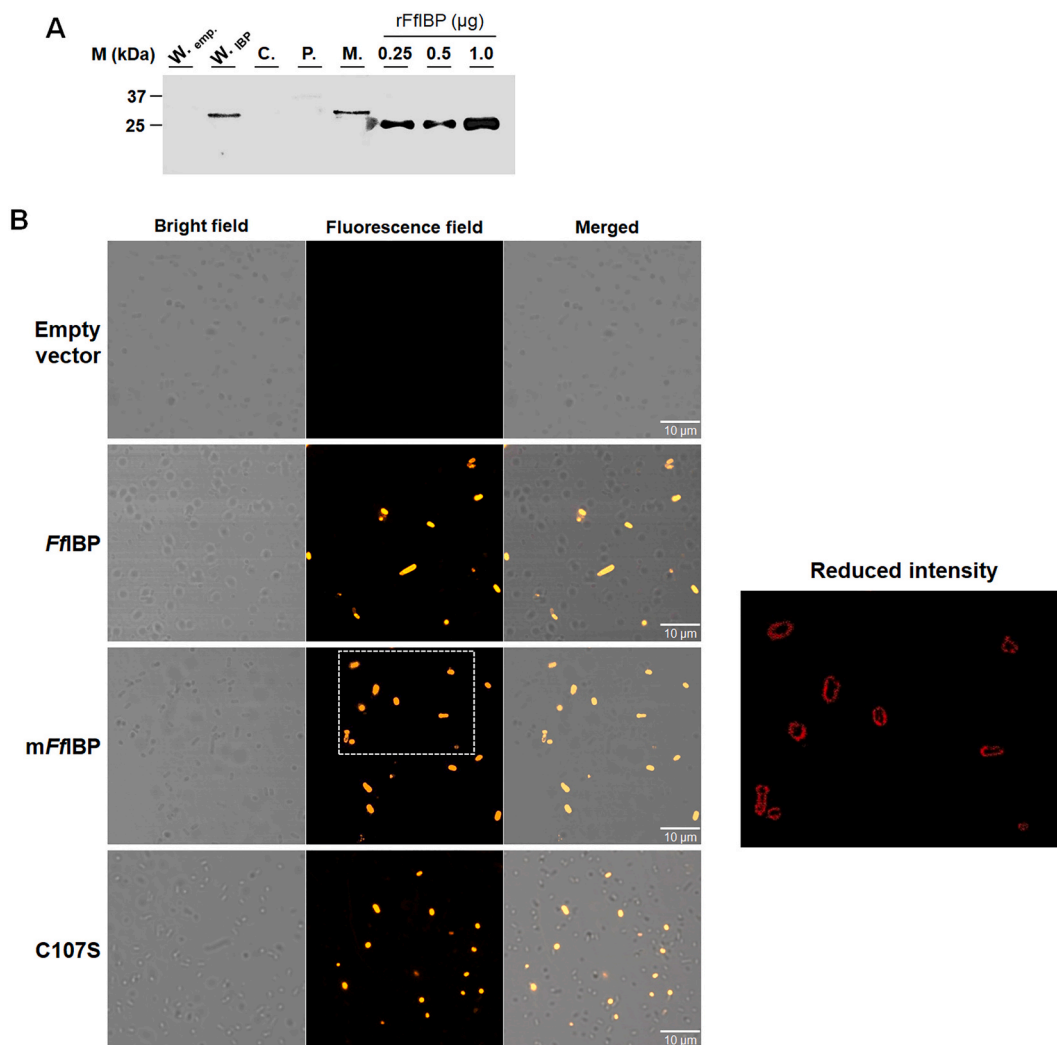


Fig. 7. Expression and identification of the subcellular localization of *FfIBP* in bacteria. (A) Western immunoblot analysis of *FfIBP* from bacterial cell fractions detected using His-tag antibodies. Cell fractions are shown above the lanes: W., whole cell; C., cytoplasm; P., periplasm; M., membrane fractions. The whole cells with empty vector (W. emp.) were considered as a negative control. Different amounts of recombinant *FfIBP* (amino acids 27–276) with His-tag were used as a positive control [11]. (B) Confocal microscopy images of cells harboring empty, *FfIBP*, *mFfIBP*, and C107S vectors. Protein-expressing bacteria were incubated with Ni-NTA-ATTO 550, washed, and examined under fluorescence microscope LSM800. Scale bars represent 10 μ m. The image from the *mFfIBP* sample with low laser intensity was shown in the right panel to identify the specific localization of IBPs.

2.5. *FflBP* is a membrane-anchored protein

To explore the benefits of IBP with hyper-TH activity in bacteria, we first analyzed the *FflBP* sequence. The sequence analysis of *FflBP* using SignalP 5.0 [36] predicted that *FflBP* has a lipoprotein signal sequence at the N-terminal of the coding sequence with 99% possibility, followed by a cysteine residue. The signal sequence has the most conserved amino acid (leucine) in the lipobox and cleaves between the LMTN and CSND sequences of the 20th amino acid (S5 Table). This sequential feature indicates *FflBP* is anchored to membranes via N-terminal lipids.

To prove that *FflBP* is a membrane-anchored protein based on signal sequence analysis, we cloned the full-length *fflbp* coding sequence in the pET-21b vector to generate C-terminal His-tagged IBPs. IBP-induced cells were then analyzed for protein expression using western blotting probed with a His-tag antibody. Subsequently, we investigated the subcellular localization of *FflBP* by fractionation. Consistent with the sequential predictions, *FflBP* was detected only in the membrane fraction (Fig. 7A).

In addition, IPTG-induced cells were incubated with $6\times$ His-tag specific fluorescent dye (NTA-Atto 550) and checked for protein localization using a fluorescence microscope. The fluorescence signal was present in the bacterial cells harboring pET21b, *FflBP*, *mFflBP*, and C107S, whereas no fluorescent signal was observed in the cells containing empty pET-21b (Fig. 7B). Moreover, the reduced fluorescent signal image revealed that the fluorescent signal was from the membrane fraction. It is noteworthy that the fluorescence dye NTA-Atto 550 is not membrane permeable. Together, these results confirm *FflBP* is a membrane-anchored protein that is most similar to the membrane of *Flavobacterium frigoris* PS1 in its natural state.

2.6. Benefits of hyperactive IBPs for microorganisms inhabiting ice

To better understand how microorganisms with IBP on their

membrane surface survive in a cold environment, the recovery rate of cells after repeated freezing and thawing processes was measured. The proteins were expressed on the cell surface and the protein expression in each cell was confirmed by checking the fluorescence level before the experiment. The first round of freeze-thaw cycles resulted in a steep decline in the recovery rates of all strains, indicating high fragility of the cells. However, differences could be observed among the strains. After the first freeze-thaw cycle, the colony forming units (CFUs) of viable bacteria with the empty vector were 3.5×10^4 on an average, whereas for the strains with *FflBP*, *mFflBP*, and C107S, the CFUs were over 7.2×10^5 , 1.7×10^6 , and 2.1×10^5 , respectively. Strains with *FflBP* had a 20 times higher survival rate than the empty vector strain. Most cells with empty vectors died in the second freeze-thaw cycle (CFU $< 1 \times 10^2$), whereas the CFUs of strains with *FflBP*, *mFflBP*, and C107S were 8.5×10^4 , 4.0×10^3 , and 5.9×10^2 , respectively. These results indicate that the cells with IBPs having a high TH activity were resistant to the repetitive freeze-thaw cycles compared with the cells without IBP (Fig. 8A).

Although the same process and conditions were used for protein expression and incubation for tagging a specific fluorescence dye, the intensity of fluorescence for each cell type was different (as shown in Fig. 7). For instance, some cells had no fluorescence, indicating variability in the protein contents in each cell, potentially because of the different IPTG-induction times for each cell. Because *FflBP* contributes to bacterial cell survival in the freeze-thaw cycle, we speculated that strains with higher *FflBP* content (high Atto fluorescence intensity) survive better than those with low or no protein content. Consistent with our hypothesis, the percentage of cells with *FflBP* (cells with fluorescence/total cells) increased from $\sim 20\%$ up to 65% after the third cycle, indicating that the strains with high *FflBP* content has a higher survival rate in the repeated freeze-thaw process than the strains without/low *FflBP* content (Fig. 8B). This could also explain the low survival rate of strains compared with those with *FflBP* in the first round of the freeze-

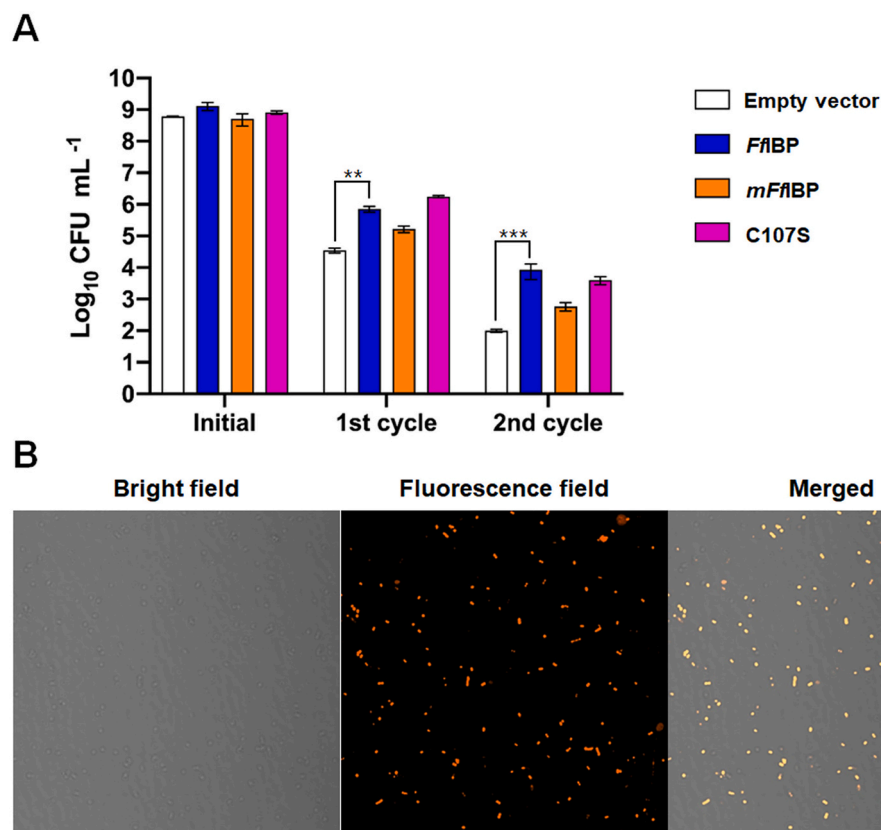


Fig. 8. CFUs of bacteria (empty, *FflBP*, *mFflBP*, and C107S) after freeze-thaw cycles. (A) The CFUs of each sample were measured after the freeze-thaw cycle to calculate the live cells. Protein-expressing cells were washed with 150 mM NaCl and the CFU was adjusted to 10^9 for the initial amount of cells. The data was plotted from three individual measurements. (B) The cells with *FflBP* that survived the 3rd freeze-thaw cycle. Cells were treated with Atto 550 for the IBP identification. Scale bar represents 10 μm .

thaw cycle.

Next, we mimicked the natural conditions to understand the detailed mechanism of bacterial survival with IBPs in ice. Cells with or without membrane-anchored IBPs were frozen in a chamber, and the morphological phenomena of ice were compared. As shown in Fig. 9 and S5 Fig., the cells (fluorescein isothiocyanate [FITC]-stained) without IBP or with *mFfIBP* (moderately active) showed high fluorescence intensity at the triangular junction of ice granules, indicating concentrated cells. In contrast, the cells with *FfIBP* or C107S were distributed in the ice and formed small brine pockets in the granule boundary with low fluorescence intensity. Smaller granules were also found in the ice cubes. Under freezing temperatures, the ice nuclei formed randomly and grew until the space was filled with ice. During this process, the cells were pushed by growing ice granules and concentrated in the triangular junction where the three ice granules were in contact. However, cells with hyperactive IBPs could attach to the ice surface and create brine pockets in the ice granule boundary. These brine pockets contained less concentrated cells and facilitated cellular distribution throughout the ice cubes. This is probably because the hyperactive IBPs bind to the multiple planes of ice and immobilize the bacteria from flowing through the quasi-liquid layer (QLL). Therefore, cells with hyperactive IBPs can be deconcentrated in ice and expand the overall living area.

To understand the beneficial effect of brine pockets on the ecological conditions of the *FfIBP* sample, we estimated the salt concentration of the ice cubes with cells using Raman spectroscopy. Previously, the OH stretching band of water was chosen to measure the dynamic properties and the effect of ions [37]. The intramolecular OH bonds are influenced

by local conditions, including the presence of ions. In the aqueous solutions, “disordered” vibration from OH-Cl was dominantly exhibited in the 3400–3600 cm^{-1} region of the Raman spectrum rather than the “ordered” vibration at 3140 cm^{-1} from accumulated water (i.e., ice) or ion-free conditions. Therefore, the salt concentration of the area of interest in the frozen sample can be estimated by calculating the Raman intensity ratio of 3140/3430 cm^{-1} . The intensity ratio of the QLL region where NaCl was mainly gathered was 1.87 in the presence of 50 mM NaCl solution, and it decreased as the NaCl concentration increased (S6 Fig.). The average ratio (3140/3430 cm^{-1}) of the 10 QLL regions with *FfIBP* was 1.42, which was higher than that of the empty sample (1.30), indicating that the salt concentration of the *FfIBP* sample in the QLL region was lower than that of the empty sample. In addition, the brine pocket region with *FfIBP* is adjacent to 1.66, whereas the empty sample is 2.08, which is close to the ratio of the ice granule region (2.07). The increased number of brine pockets and smaller ice granules probably helped expand the area of the QLL region and reduced the salt concentration. These results suggest that cells with *FfIBP* are exposed to mild salt concentration in QLL and brine pockets under freezing conditions, whereas those without *FfIBP* experience extreme conditions (high salt at QLL; or ice in the brine or bubble region) (Fig. 10 and S7 Fig.).

3. Discussion

Many IBPs have been found in plants, animals, insects, fungi, and bacteria [38]. Structural and biochemical investigations helped us understand the ice-binding mechanisms of these proteins. Although

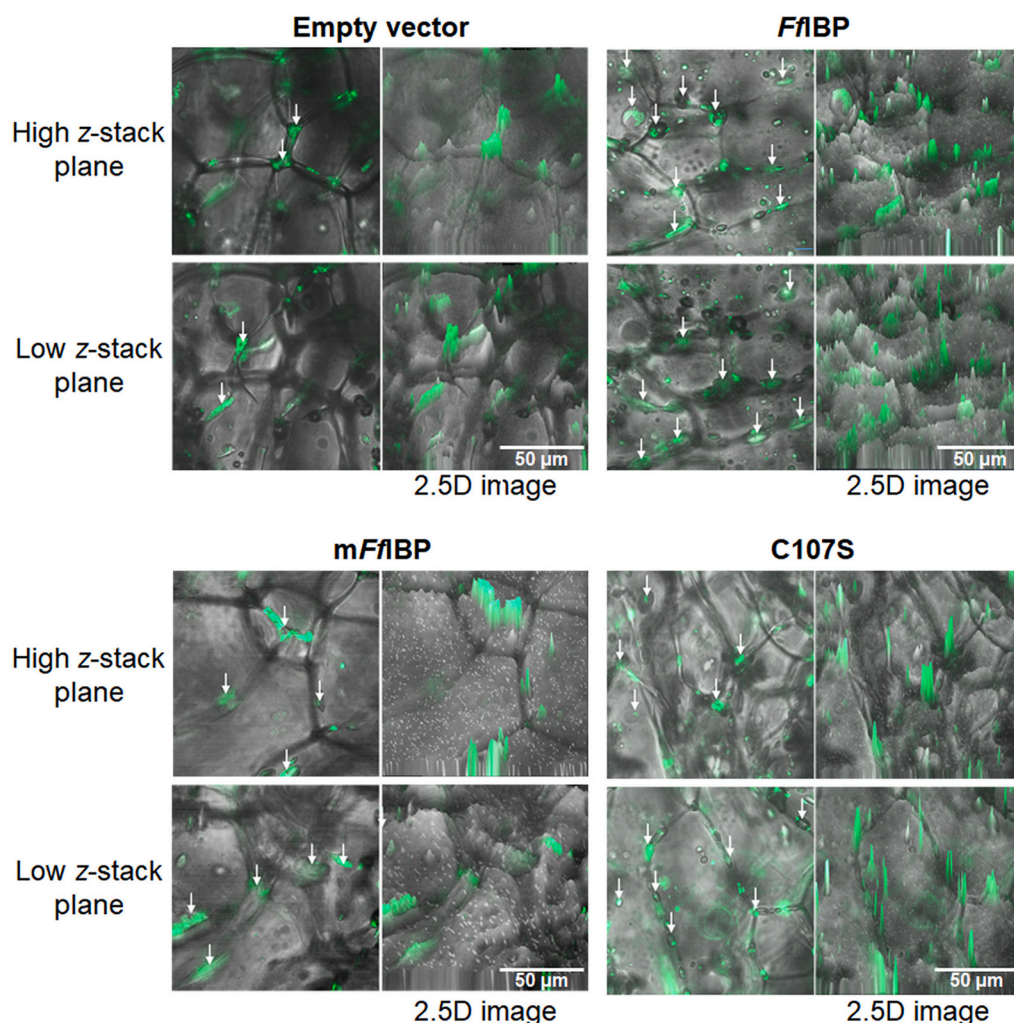


Fig. 9. Confocal microscopy of ice-trapped bacterial cells. Bacteria were frozen in a 1 cm × 1 cm chamber and observed using a fluorescence microscope. The intensity of fluorescence was indicated vertically in the 2.5-dimension (2.5D) images on the right of each image. Different levels along the z-axis were observed in the same system (lower panel). Images shown are merged bright field and fluorescence field images. Concentrated cells, either in the triangular junction of ice or brine pockets, are indicated with white arrows. Scale bar represents 50 μm.

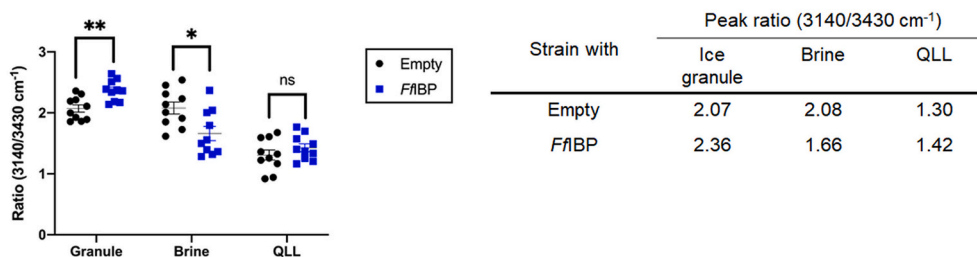


Fig. 10. Peak ratio of Raman spectroscopy (3140/3430 cm⁻¹). The 10 ice granules, brine pockets, and QLL region areas were scanned five times and averaged. The averaged data indicated on the right correspond to the data in the graph. A single asterisk [*] indicates *p* < 0.05, and double asterisks [**] indicate *p* < 0.01 by unpaired *t*-test. ns: not significant.

uncertainty remains regarding the ice-binding mechanism due to the structural diversity of IBPs [32,34], numerous studies indicate that IBPs interact with ice via the “ice-like waters” that are layers of water molecules on IBS [15,27]. These water molecules can be arranged by interactions involving hydrogen bonding and hydrophobic effects to facilitate the interaction with ice. *FfIBP* also has a hydrophobic surface

with spaced hydroxyl groups from the motifs, which is not only considered crucial for locating the polygonally arranged ice-like water molecules on IBS, but is also directly related to the TH activity (Fig. 1B) [27].

IBPs are divided into two categories based on their TH activity: moderate and hyperactive IBPs. However, the mechanism underlying

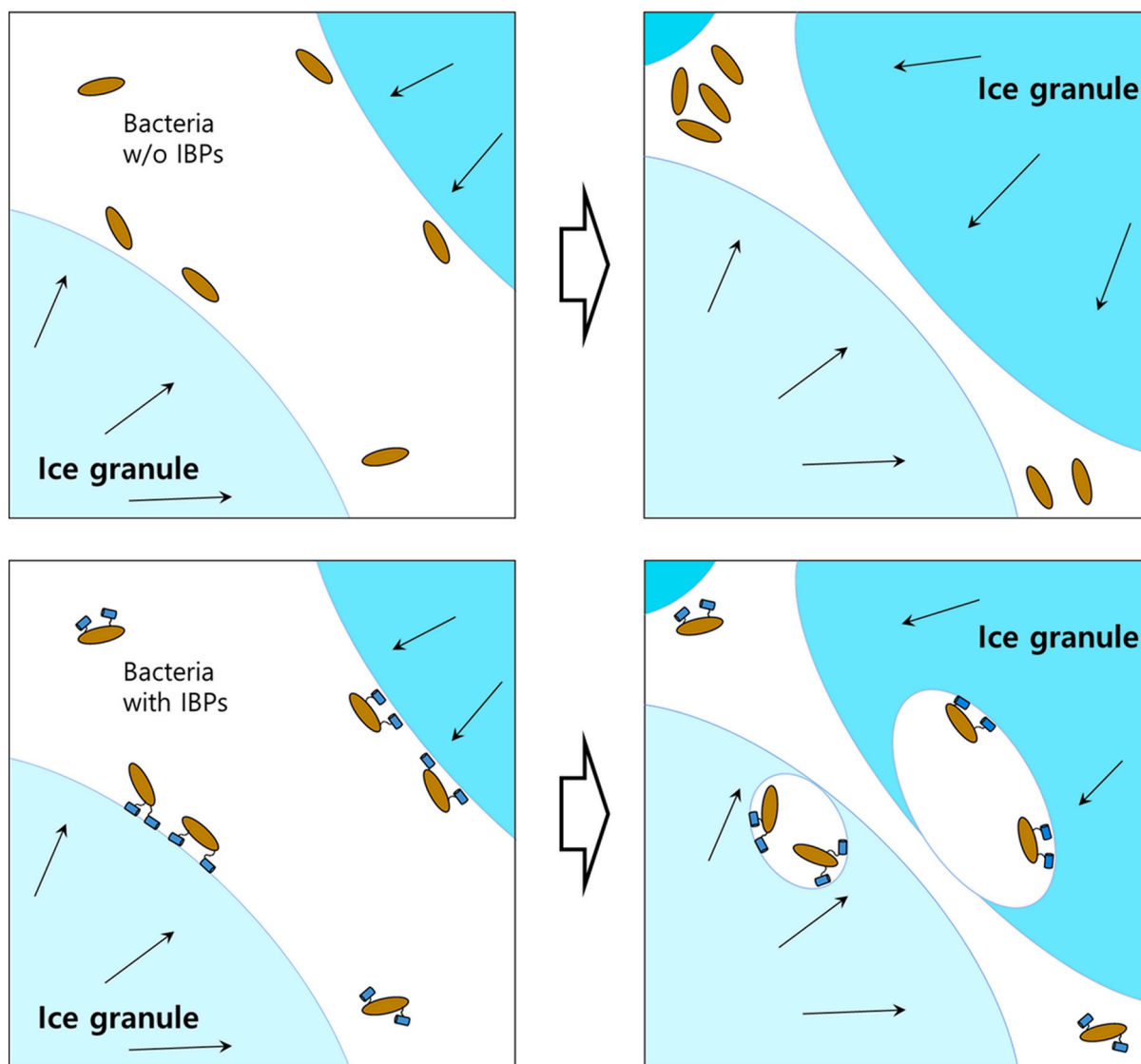


Fig. 11. Proposed survival mechanism of bacteria with membrane-anchored IBP. (Top) Bacteria without IBPs on the ice surface were flown into the triangular junction of ice granules and concentrated with salt. (Bottom) Bacteria with IBPs bound to the ice surface using the IBPs inhibit ice growth and form brine pockets as individual habitats. The ice granules are shown in cyan. The bacteria and IBPs are indicated with brown ovals and blue cylinders, respectively. (For interpretation of the references to color in this figure legend, the reader is referred to the web version of this article.)

these differences in activity is yet to be elucidated. Here, we report hyperactive *FfIBP* has a unique capping head region with a disulfide bond, which stabilizes the protein and reduces the movement of residues at the IBS. The movement of residues on IBPs can be negatively correlated with TH activity. Replacing the capping region or breaking the disulfide bond on the capping region caused incremental fluctuation of residue T79 and orientation of side chains of residues on IBS, which may destabilize the hydration water layer and decrease the TH activity.

The correlation between structural stability and TH activity can be found in other IBPs. Unlike moderate IBPs, hyperactive IBPs either have disulfide bond(s) between the β -strands or *FfIBP*-like-capping head region. The disulfide bond(s) maintains a regular space among strands, which minimizes residual fluctuation in the IBS and most likely increases the strength with a long-range interaction time between the IBP and ice, resulting in hyperactivity. Thus, structural stability constitutes another condition for IBP to be hyperactive. These novel insights into the complexities of the ice-binding mechanism of IBPs will provide new evidence for distinguishing IBPs into moderate and hyperactive IBPs, predicting information on the activity of uncharacterized IBPs and ideas for the generation of artificial IBPs for hyperactivity.

Another key finding of this study is the role of membrane-anchored hyperactive IBPs in cold environments. All previously characterized DUF3494 IBP family members are secreted and thought to secure the area by inhibiting ice growth toward the bacterial habitat (S5 Table) [39,40]. The reason that only secretory IBPs have been discovered is probably that researchers initially screened IBPs from the bacterial secretome. Unlike these IBPs, *FfIBP* is a membrane-anchored protein not yet characterized. Bacteria with *FfIBP* can effectively survive freeze-thaw cycles. Experiments mimicking natural conditions indicate *FfIBP* induces the formation of brine pockets by preventing the migration of bacteria in the QLL (Figs. 9 and 11). The number of brine pockets depends on the TH activity. Multiple ice-binding sites—characteristic features of hyperactive IBPs—probably help bacteria bind to various planes on the ice boundary and generate brine pockets starting from the ice-bound bacteria (Fig. 11). The generation of brine pockets could be beneficial for the short- and long-term survival of bacteria. An increase in brine pocket domains reduces salt concentration in QLL and brine pockets, protecting bacteria from osmotic shock during the freezing process [41]. The freezing process accompanies increases in solute concentrations in the liquid-like layer of ice. The high salt concentration outside the cell induces the migration of the water through biological membranes, and microorganisms living in this condition have to adapt their physiology to maintain a high osmotic pressure. Especially the rapid change in salt concentration occurring in the freezing process is harsher for the microorganisms. Therefore, maintaining the low salt concentration in the extended QLL or brine pocket will help the organisms in living in the polar region.

Another advantage of brine pockets is nutrient acquisition by bacteria. The polar microorganisms in the ice experience a nutrient limitation [42]. This distribution of trapped bacteria with a low population in the habitat is probably beneficial for the bacteria to reduce the nutrient consumption for long-term survival compared to the concentrated population in the brine pocket (Fig. 11). We also found that several uncovered or uncharacterized IBPs in bacteria from the cold environment have a lipoprotein signal peptide sequence at the N-terminal (S8 Fig.). This observation indicates that the survival mechanism with membrane-anchored IBPs and generation of brine pockets, as suggested in this study, is another example of the cold-adaptation mechanism of microorganisms from the polar region.

In conclusion, the findings in this study provide a detailed molecular and mechanistic understanding of the relationship between residual rigidity and TH activity. The rigidity of IBP stemming from the capping head region, especially the disulfide bond, can immobilize the residues at the IBS to increase the protein-ice interaction strength, as indicated by hyper-TH activity. Furthermore, cells with IBPs on the membrane surface survive better than cells without IBPs by generating brine pockets to

expand the living space in a TH activity-dependent manner. Thus, we identified a previously unknown survival mechanism using membrane-anchored IBPs responsible for polar microorganism survival in a cold environment.

4. Materials and methods

4.1. Purification of IBPs

Recombinant *FfIBP* and *mFfIBP* were obtained as previously described [10,21]. The *FfIBP* gene in the pCold vector was transformed into BL21(DE3) cells. Overnight seed culture from a single cell was inoculated into 4 L of Luria–Bertani (LB) broth supplemented with ampicillin. Once the culture reached an OD_{600} of 0.8, 1 mM IPTG was added to induce protein expression for 36 h at 10 °C. The cells were harvested by centrifugation, and the proteins were purified by His-tag purification followed by FPLC using a HiLoad® 16/600 Superdex® 200 pg column. Similar protein expression and purification methods were applied to the C107S mutant construct. For *mFfIBP* protein production, a pET28a vector was used, and protein production was induced at 25 °C (S1 Table).

4.2. Circular dichroism analysis

The secondary structure composition of *FfIBP*, *mFfIBP* and C107S were determined using circular dichroism analysis. The far-UV CD was performed using a Chirascan CD spectrometer (Applied Photophysics Ltd., Leatherhead, UK) between 200 and 260 nm using a quartz cuvette with 1 mm path length at 293 K. Five scans were recorded, the baseline spectra (buffer alone) were subtracted and the results were averaged followed by smoothing of the data. Buffer used for the proteins was 20 mM Tris pH 8.5, 150 mM NaCl.

4.3. Structure determination and models for MD simulation

The structure of C107S was determined by X-ray crystallography. The purified protein was crystallized using the hanging drop vapor diffusion method with a precipitant solution composed of sodium citrate pH 4.6 and 2.9 M NaCl. The crystal was diffracted at 2.0 Å, and the structure phase was obtained by molecular replacement using the *FfIBP* crystal structure (PDB code: 4NU2). The refined C107S structure was almost identical to *FfIBP*, as indicated by the RMSD value of 0.158, except for the disulfide bond. The detailed data after refinement are listed in S2 Table (PDB CODE: 7EHK). The crystal structures of *FfIBP* (PDB: 4NU2, 2.1 Å resolution), C107S, and chimeric *mFfIBP* (PDB: 4NU3, 1.4 Å resolution) (chain A) were used as models for the MD simulations. Water molecules and ions obtained from the crystallographic studies were removed.

4.4. MD simulation

The protein structures were subjected to MD simulations using GROMACS v2020.4 with the CHARMM 27 force field topologies and parameters [43,44]. Process and syntax followed the GROMACS documentation and the Galaxy platform [44]. The system was solvated with a TIP4P water model in a cubic box and neutralized with 0.15 M NaCl. The dimension of sides of the cubic box was 4 nm for each system, and the model was located at the center of the box before the simulation. One thousand steps of the steepest descent followed by 50,000 steps of the adopted basis Newton-Raphson method were performed for minimization. Two equilibrations steps—isoenthalpic-isochoric ensemble (NVT; the number of particles (N), simulation cell volume (V), and temperature (T)) and the isothermal-isobaric ensemble (NPT; pressure (P))—were performed for 4 ns before the production step. In addition, a leap-frog algorithm for integrating Newton motion equation and a smooth particle mesh Ewald (SPME) method for electrostatic and van der Waals

interactions were applied [45]. MD was performed at 300 K with a 1-fs time step for 50 ns (simulated 2 ns.gro trajectory output files, which were continuously restarted by the res-files, were combined into the final 50 ns) under the NPT ensemble. GROMACS v2020.4 and parameter sets were used to run MD simulation. GROMACS was used to analyze the trajectory files for RMSD, RMSF, the distances between residues, and the side-chain distribution. The VMD and Pymol programs were used for figure generation.

4.5. TH activity

The ice morphology at freezing points was obtained during the measurement of the TH activity of IBPs, as described previously [10]. Briefly, the sample was placed on holes of an aluminum disk on the stage and frozen rapidly at approximately $-20\text{ }^{\circ}\text{C}$ using a nanoliter osmometer (Otago Osmometers, Dunedin, New Zealand). The temperature was raised slowly until a single ice crystal remained (melting temperature). The temperature was then lowered again slowly ($\sim 0.5\text{ }^{\circ}\text{C}/\text{min}$) until the ice crystal grew (freezing temperature). The morphology of the ice crystals at the freezing point was observed under a microscope. Images were taken using a Canon Power Shot 620. Measurements were performed in 20 mM Tris-HCl (pH 8.5) and 150 mM NaCl buffer at various sample concentrations.

4.6. Expression and localization of IBPs

Genes for IBPs (full-length *FfIBP*, *mFfIBP*, and *C107S*) were cloned into pET-21b at the *NdeI* restriction enzyme site using the LIC cloning method [46] to generate C-terminal His-tagged IBPs. BL21(DE3) cells were transformed with cloned vectors. IPTG (1 mM) was added to the culture medium at an OD_{600} of 0.5 and incubated for 20 h to induce protein expression. The cells were then washed three times with phosphate-buffered saline (PBS) or 150 mM NaCl three times and incubated with His-tag specific fluorescence dye (Ni-NTA-Atto 550; Sigma-Aldrich, St. Louis, MO, USA) for 15 min. The unbound fluorescence dye was washed twice with PBS or 150 mM NaCl. The protein expression levels and localization were analyzed using a microplate reader (EnVision 2013 multilabel Reader; Perkin Elmer, Waltham, MA, USA) or under a laser confocal microscope (LSM-800; Zeiss, Oberkochen, Germany).

4.7. Subcellular fractionation

Subcellular fractionation was followed by a combination of cold osmotic shock and sonication methods, named PureFrac [47]. IPTG-induced cells were washed twice with PBS and centrifuged, and the supernatant was discarded. The cell pellet was resuspended in a spheroplast buffer (0.1 M Tris-HCl, pH 8.0, 500 mM sucrose, and 0.5 mM EDTA), incubated for 5 min, and the supernatant was carefully discarded after centrifugation. The pellet was then resuspended in cold 1 mM MgCl_2 , incubated for 15 s on ice, and then 20 mM MgSO_4 was added to the periplasmic fraction. The pelleted cells were resuspended in buffer (50 mM Tris-acetate, pH 8.0, 2.5 mM EDTA) and sonicated on ice. The lysed cells were centrifuged at 16,000 rpm for 40 min, and the supernatant and pellets were separated into cytoplasmic and membrane fractions, respectively.

4.8. Western blotting

Samples from subcellular fractionation were loaded onto an SDS-PAGE gel, and the proteins were semi-dry transferred to a PVDF membrane. The membrane with proteins was blocked with skim milk overnight at $4\text{ }^{\circ}\text{C}$. After blocking, the membrane was incubated with a His-probe antibody (SC-53073; SANTA CRUZ, Santa Cruz, CA, USA) at 1:2000 dilution and the m-IgGk BP-HRP (SC-516102; Santa Cruz) at 1:20,000 dilution in TBST. SuperSignal™ West Femto (Thermo Fisher,

Waltham, MA, USA) was the chemiluminescent substrate.

4.9. Recovery rate of bacteria

The protective effects of IBPs on bacteria from the freeze-thaw cycle were measured by calculating CFUs. First, the cells were washed, resuspended in 150 mM NaCl solution, and the OD_{600} was adjusted to 1.0, representing approximately 1×10^9 CFUs for all samples. Next, the cells were frozen at $-80\text{ }^{\circ}\text{C}$ without a cryoprotectant. After 1 day, the frozen cells were thawed on ice for 30 min and transferred to $25\text{ }^{\circ}\text{C}$. The serial dilutions of the samples were plated on LB agar plates for CFU calculation in the first round of the freeze-thaw cycle. The thawed cells were re-frozen and then thawed again using a similar process as the second freeze-thaw cycle next day. A similar process was used to calculate the recovery rate for the third freeze-thaw cycle.

4.10. Brine pocket formation using laser confocal microscopy

The protective effects of IBPs on bacterial cells were analyzed using a laser confocal microscope (LSM-800; Zeiss) equipped with a Linkam THMS 600 stage (Linkam Scientific Instruments, Tadworth, UK) controlled by Linksys software. IPTG-induced bacterial cells were washed twice with PBS and resuspended in 150 mM NaCl solution in the same volume of the culture medium. Thereafter, the cells were mixed with water containing 100 nM FITC at a 1:1 ratio, placed in a square chamber fitted to the Linkam THMS 600 stage, and frozen. The freezing process was performed in three steps: the temperature was first decreased from $25\text{ }^{\circ}\text{C}$ to $0\text{ }^{\circ}\text{C}$ at a rate of $-5\text{ }^{\circ}\text{C}/\text{min}$, and then decreased to $-5\text{ }^{\circ}\text{C}$ at a rate of $1\text{ }^{\circ}\text{C}/\text{min}$, and finally to $-20\text{ }^{\circ}\text{C}$ at a rate of $-0.2\text{ }^{\circ}\text{C}/\text{min}$. The temperature was maintained for 30 s between the steps for latent heat. The FITC (detection wavelength 490–700 nm) and electronically switchable illumination and detection (ESID) channels were observed using LSM-800 with an LD $\times 50$ objective ($N/A = 0.55$) with a 488 nm laser as the excitation source. A GaAsP-PMT detector for the FITC channel and photodiode ESID detector for the ESID channel were used.

4.11. Raman spectroscopy of brine pocket and QLL

Confocal Raman spectroscopy (inVia Qontor; Renishaw, Wotton-under-Edge, UK) was used to investigate the relative salt concentrations in the brine pockets. An aqueous NaCl solution with different salt concentrations was dropped onto a temperature-controlled stage, followed by a reduction rate of $-0.2\text{ }^{\circ}\text{C}/\text{min}$ to $-20\text{ }^{\circ}\text{C}$. The detailed freezing process with cells was similar to that used in processing the samples for laser confocal microscopy, except for adding FITC. After the temperature reached $-20\text{ }^{\circ}\text{C}$, the ice granules, brine pockets, and QLL regions were scanned from 2868 to 3693 cm^{-1} . The spectra from 10 areas were scanned five times and averaged. A 532 nm laser was used as the excitation source. The salt concentration of the aqueous solution was estimated to proximate the brine pocket, and the QLL region was measured by Raman spectroscopy, as shown previously [37].

Accession number

PDB: 7EHK.

Funding information

This research was part of the project titled “Development of potential antibiotic compounds using polar organism resources” (grant no. 15250103, KOPRI grant PM22030), funded by the Ministry of Oceans and Fisheries, Korea. This work was also supported by the Korea Polar Research Institute (KOPRI; grant numbers PE22160, PE22120, and PE21300).

CRedit authorship contribution statement

Jisub Hwang: Data curation, Formal analysis, Methodology, Validation, Visualization, Writing – original draft. **Bomi Kim:** Data curation, Formal analysis, Methodology, Validation, Visualization, Writing – original draft. **Min Ju Lee:** Data curation, Formal analysis. **Eun Jae Kim:** Methodology, Resources. **Sung Mi Cho:** Methodology, Resources. **Sung Gu Lee:** Validation, Visualization. **Se Jong Han:** Formal analysis. **Kitae Kim:** Conceptualization, Funding acquisition, Investigation, Resources, Supervision, Writing – review & editing. **Jun Hyuck Lee:** Conceptualization, Funding acquisition, Investigation, Project administration, Supervision, Writing – review & editing. **Hackwon Do:** Conceptualization, Funding acquisition, Investigation, Project administration, Supervision, Writing – original draft, Writing – review & editing.

Declaration of competing interest

The authors declare no competing interests.

Acknowledgments

We would like to thank the staff at the X-ray core facility of the Korea Basic Science Institute (KBSI; Ochang, Korea) and the BL-5C of the Pohang Accelerator Laboratory (Pohang, Korea) for their kind help with X-ray diffraction data collection.

Appendix A. Supplementary data

Supplementary data to this article can be found online at <https://doi.org/10.1016/j.ijbiomac.2022.02.032>.

References

- H.J. Kim, J.H. Lee, Y.B. Hur, C.W. Lee, S.H. Park, B.W. Koo, Marine antifreeze proteins: structure, function, and application to cryopreservation as a potential cryoprotectant, *Mar. Drugs* 15 (2017), <https://doi.org/10.3390/md15020027>.
- C.A. Knight, A.L. DeVries, L.D. Oolman, Fish antifreeze protein and the freezing and recrystallization of ice, *Nature* 308 (1984) 295–296, <https://doi.org/10.1038/308295a0>.
- K. Muldrew, L.E. McGann, Mechanisms of intracellular ice formation, *Biophys. J.* 57 (1990) 525–532, [https://doi.org/10.1016/S0006-3495\(90\)82568-6](https://doi.org/10.1016/S0006-3495(90)82568-6).
- P. Mazur, S. Seki, I.L. Pinn, F.W. Kleinhans, K. Edashige, Extra- and intracellular ice formation in mouse oocytes, *Cryobiology* 51 (2005) 29–53, <https://doi.org/10.1016/j.cryobiol.2005.04.008>.
- K.E. Zachariassen, E. Kristiansen, Ice nucleation and antinucleation in nature, *Cryobiology* 41 (2000) 257–279, <https://doi.org/10.1006/cryo.2000.2289>.
- S. D'Amico, T. Collins, J.C. Marx, G. Feller, C. Gerday, Psychrophilic microorganisms: challenges for life, *EMBO Rep.* 7 (2006) 385–389, <https://doi.org/10.1038/sj.embor.7400662>.
- A.L. DeVries, Antifreeze glycopeptides and peptides: interactions with ice and water, *Methods Enzymol.* 127 (1986) 293–303, [https://doi.org/10.1016/0076-6879\(86\)27024-X](https://doi.org/10.1016/0076-6879(86)27024-X).
- E. Kristiansen, K.E. Zachariassen, The mechanism by which fish antifreeze proteins cause thermal hysteresis, *Cryobiology* 51 (2005) 262–280, <https://doi.org/10.1016/j.cryobiol.2005.07.007>.
- Y.C. Liou, A. Tocilj, P.L. Davies, Z. Jia, Mimicry of ice structure by surface hydroxyls and water of a β -helix antifreeze protein, *Nature* 406 (2000) 322–324, <https://doi.org/10.1038/35018604>.
- H. Do, J.H. Lee, S.G. Lee, H.J. Kim, Crystallization and preliminary X-ray crystallographic analysis of an ice-binding protein (FfIBP) from *Flavobacterium frigidum* PS1, *Acta Crystallogr. Sect. F: Struct. Biol. Cryst. Commun.* 68 (2012) 806–809, <https://doi.org/10.1107/S1744309112020465>.
- L.A. Graham, Y.C. Liou, V.K. Walker, P.L. Davies, Hyperactive antifreeze protein from beetles, *Nature* 388 (1997) 727–728, <https://doi.org/10.1038/41908>.
- C.B. Marshall, A. Chakrabarty, P.L. Davies, Hyperactive antifreeze protein from winter flounder is a very long rod-like dimer of α -helices, *J. Biol. Chem.* 280 (2005) 17920–17929, <https://doi.org/10.1074/jbc.M500622200>.
- F.H. Lin, T. Sun, G.L. Fletcher, P.L. Davies, Thermolabile antifreeze protein produced in *Escherichia coli* for structural analysis, *Protein Expr. Purif.* 82 (2012) 75–82, <https://doi.org/10.1016/j.pep.2011.11.013>.
- E.K. Leinala, P.L. Davies, D. Doucet, M.G. Tyshenko, V.K. Walker, Z. Jia, A β -helical antifreeze protein isoform with increased activity. Structural and functional insights, *J. Biol. Chem.* 277 (2002) 33349–33352, <https://doi.org/10.1074/jbc.M205575200>.
- C.P. Garnham, R.L. Campbell, P.L. Davies, Anchored clathrate waters bind antifreeze proteins to ice, *Proc. Natl. Acad. Sci. U. S. A.* 108 (2011) 7363–7367, <https://doi.org/10.1073/pnas.1100429108>.
- S.P. Graether, M.J. Kuiper, S.M. Gagné, V.K. Walker, Z. Jia, B.D. Sykes, P.L. Davies, β -helix structure and ice-binding properties of a hyperactive antifreeze protein from an insect, *Nature* 406 (2000) 325–328, <https://doi.org/10.1038/35018610>.
- A. Cheng, K.M. Merz, Ice-binding mechanism of winter flounder antifreeze proteins, *Biophys. J.* 73 (1997) 2851–2873, [https://doi.org/10.1016/S0006-3495\(97\)78315-2](https://doi.org/10.1016/S0006-3495(97)78315-2).
- M.J. Kuiper, C.J. Morton, S.E. Abraham, A. Gray-Weale, The biological function of an insect antifreeze protein simulated by molecular dynamics, *elife* 4 (2015), <https://doi.org/10.7554/eLife.05142>.
- J. Cheng, Y. Hanada, A. Miura, S. Tsuda, H. Kondo, Hydrophobic ice-binding sites confer hyperactivity of an antifreeze protein from a snow mold fungus, *Biochem. J.* 473 (2016) 4011–4026, <https://doi.org/10.1042/BCJ20160543>.
- S.M. Marks, A.J. Patel, Antifreeze protein hydration waters: unstructured unless bound to ice, *Proc. Natl. Acad. Sci. U. S. A.* 115 (2018) 8244–8246, <https://doi.org/10.1073/pnas.1810812115>.
- H. Do, S.J. Kim, H.J. Kim, J.H. Lee, Structure-based characterization and antifreeze properties of a hyperactive ice-binding protein from the Antarctic bacterium *Flavobacterium frigidum* PS1, *Acta Crystallogr. D Biol. Crystallogr.* 70 (2014) 1061–1073, <https://doi.org/10.1107/S1399004714000996>.
- K.S. Park, H. Do, J.H. Lee, S.I. Park, E.J. Kim, S.J. Kim, S.H. Kang, H.J. Kim, Characterization of the ice-binding protein from Arctic yeast *leucosporidium* sp. AY30, *Cryobiology* 64 (2012) 286–296, <https://doi.org/10.1016/j.cryobiol.2012.02.014>.
- J.H. Lee, A.K. Park, H. Do, K.S. Park, S.H. Moh, Y.M. Chi, H.J. Kim, Structural basis for antifreeze activity of ice-binding protein from arctic yeast, *J. Biol. Chem.* 287 (2012) 11460–11468, <https://doi.org/10.1074/jbc.M111.331835>.
- A. Hudait, N. Odendahl, Y. Qiu, F. Paesani, V. Molinero, Ice-nucleating and antifreeze proteins recognize ice through a diversity of anchored clathrate and ice-like motifs, *J. Am. Chem. Soc.* 140 (2018) 4905–4912, <https://doi.org/10.1021/jacs.8b01246>.
- S. Chakraborty, B. Jana, Optimum number of anchored clathrate water and its instantaneous fluctuations dictate ice plane recognition specificities of insect antifreeze protein, *J. Phys. Chem. B* 122 (2018) 3056–3067, <https://doi.org/10.1021/acs.jpcc.8b00548>.
- E. Jurrus, D. Engel, K. Star, K. Monson, J. Brandi, L.E. Felberg, D.H. Brookes, L. Wilson, J. Chen, K. Liles, M. Chun, P. Li, D.W. Gohara, T. Dolinsky, R. Konecny, D.R. Koes, J.E. Nielsen, T. Head-Gordon, W. Geng, R. Krasny, G.W. Wei, M.J. Holst, J.A. McCammon, N.A. Baker, Improvements to the APBS biomolecular solvation software suite, *Protein Sci.* 27 (2018) 112–128, <https://doi.org/10.1002/pro.3280>.
- A. Yamauchi, T. Arai, H. Kondo, Y.C. Sasaki, S. Tsuda, An ice-binding protein from an Antarctic ascomycete is fine-tuned to bind to specific water molecules located in the ice prism planes, *Biomolecules* 10 (2020) 1–15, <https://doi.org/10.3390/biom10050759>.
- A.Q. Zhou, C.S. O'Hern, L. Regan, The power of hard-sphere models: explaining side-chain dihedral angle distributions of the α and β , *Biophys. J.* 102 (2012) 2345–2352, <https://doi.org/10.1016/j.bpj.2012.01.061>.
- Y. Celik, L.A. Graham, Y.F. Mok, M. Bar, P.L. Davies, I. Braslavsky, Superheating of ice crystals in antifreeze protein solutions, *Proc. Natl. Acad. Sci. U. S. A.* 107 (2010) 5423–5428, <https://doi.org/10.1073/pnas.0909456107>.
- A.J. Scotter, C.B. Marshall, L.A. Graham, J.A. Gilbert, C.P. Garnham, P.L. Davies, The basis for hyperactivity of antifreeze proteins, *Cryobiology* 53 (2006) 229–239, <https://doi.org/10.1016/j.cryobiol.2006.06.006>.
- T.D.R. Vance, L.A. Graham, P.L. Davies, An ice-binding and tandem beta-sandwich domain-containing protein in *shewanella frigidimarina* is a potential new type of ice adhesin, *FEBS J.* 285 (2018) 1511–1527, <https://doi.org/10.1111/febs.14424>.
- M. Bayer-Giraldi, G. Sasaki, K. Nagashima, S. Kipfstuhl, D.A. Vorontsov, Y. Furukawa, Growth suppression of ice crystal basal face in the presence of a moderate ice-binding protein does not confer hyperactivity, *Proc. Natl. Acad. Sci. U. S. A.* 115 (2018) 7479–7484, <https://doi.org/10.1073/pnas.1807461115>.
- Y. Hanada, Y. Nishimiya, A. Miura, S. Tsuda, H. Kondo, Hyperactive antifreeze protein from an Antarctic sea ice bacterium *colwellia* sp. has a compound ice-binding site without repetitive sequences, *FEBS J.* 281 (2014) 3576–3590, <https://doi.org/10.1111/febs.12878>.
- P.L. Davies, Ice-binding proteins: a remarkable diversity of structures for stopping and starting ice growth, *Trends Biochem. Sci.* 39 (2014) 548–555, <https://doi.org/10.1016/j.tibs.2014.09.005>.
- M. Mangiagalli, G. Sarusi, A. Kaleda, M. Bar Dolev, V. Nardone, V.F. Vena, I. Braslavsky, M. Lotti, M. Nardini, Structure of a bacterial ice binding protein with two faces of interaction with ice, *FEBS J.* 285 (2018) 1653–1666, <https://doi.org/10.1111/febs.14434>.
- J.J. Almagro Armenteros, K.D. Tsirigos, C.K. Sønderby, T.N. Petersen, O. Winther, S. Brunak, G. von Heijne, H. Nielsen, SignalP 5.0 improves signal peptide predictions using deep neural networks, *Nat. Biotechnol.* 37 (2019) 420–423, <https://doi.org/10.1038/s41587-019-0036-z>.
- I. Đuričković, M. Marchetti, R. Claverie, P. Bourson, J.M. Chassot, M.D. Fontana, Experimental study of NaCl aqueous solutions by raman spectroscopy: towards a new optical sensor, *Appl. Spectrosc.* 64 (2010) 853–857, <https://doi.org/10.1366/000370210792080984>.
- I.K. Voets, From ice-binding proteins to bio-inspired antifreeze materials, *Soft Matter* 13 (2017) 4808–4823, <https://doi.org/10.1039/c6sm02867e>.
- H.J. Kim, J.H. Lee, H. Do, W. Jung, Production of Antifreeze Proteins by Cold-adapted Yeasts, 2014, https://doi.org/10.1007/978-3-642-39681-6_12.

- [40] K. Junge, J.T. Staley, *Extremophiles Handbook*, Extrem. Handb, 2011, <https://doi.org/10.1007/978-4-431-53898-1>.
- [41] M. Ewert, J.W. Deming, Bacterial responses to fluctuations and extremes in temperature and brine salinity at the surface of Arctic winter sea ice, *FEMS Microbiol. Ecol.* 89 (2014) 476–489, <https://doi.org/10.1111/1574-6941.12363>.
- [42] H. Kuosa, H. Kaartokallio, Experimental evidence on nutrient and substrate limitation of Baltic Sea sea-ice algae and bacteria, *Hydrobiologia* 554 (2006) 1–10, <https://doi.org/10.1007/s10750-005-1001-z>.
- [43] M.J. Abraham, T. Murtola, R. Schulz, S. Páll, J.C. Smith, B. Hess, E. Lindahl, Gromacs: high performance molecular simulations through multi-level parallelism from laptops to supercomputers, *SoftwareX* 1–2 (2015) 19–25, <https://doi.org/10.1016/j.softx.2015.06.001>.
- [44] E. Afgan, D. Baker, B. Batut, M. Van Den Beek, D. Bouvier, M. Cech, J. Chilton, D. Clements, N. Coraor, B.A. Grüning, A. Guerler, J. Hillman-Jackson, S. Hiltmann, V. Jalili, H. Rasche, N. Soranzo, J. Goecks, J. Taylor, A. Nekrutenko, D. Blankenberg, The Galaxy platform for accessible, reproducible and collaborative biomedical analyses: 2018 update, *Nucleic Acids Res.* 46 (2018), <https://doi.org/10.1093/nar/gky379>. W537–W544.
- [45] U. Essmann, L. Perera, M.L. Berkowitz, T. Darden, H. Lee, L.G. Pedersen, A smooth particle mesh ewald method, *J. Chem. Phys.* 103 (1995) 8577–8593, <https://doi.org/10.1063/1.470117>.
- [46] J.Y. Jeong, H.S. Yim, J.Y. Ryu, H.S. Lee, J.H. Lee, D.S. Seen, S.G. Kang, One-step sequence- and ligation-independent cloning as a rapid and versatile cloning method for functional genomics studies, *Appl. Environ. Microbiol.* 78 (2012) 5440–5443, <https://doi.org/10.1128/AEM.00844-12>.
- [47] G. Malherbe, D.P. Humphreys, E. Davé, A robust fractionation method for protein subcellular localization studies in *Escherichia coli*, *BioTechniques* 66 (2019) 171–178, <https://doi.org/10.2144/btn-2018-0135>.
- [48] A. Białkowska, E. Majewska, A. Olczak, A. Twarda-clapa, Ice binding proteins: diverse biological roles and applications in different types of industry, *Biomolecules* 10 (2020), <https://doi.org/10.3390/biom10020274>.